IAEA nuclear fusion

Validation of the ERO2.0 code using W7-X and JET experiments and predictions for ITER operation

To cite this article: J. Romazanov *et al* 2024 *Nucl. Fusion* **64** 086016

OPEN ACCESS
IOP Publishing | International Atomic Energy Agency Nuclear Fusion
Nucl. Fusion **64** (2024) 086016 (11pp) https://doi.org/10.1088/1741-4326/ad5368

Validation of the ERO2.0 code using W7-X and JET experiments and predictions for ITER operation

J. Romazanov[1,10,*], S. Brezinsek[1,2], C. Baumann[1], S. Rode[1,2], A. Kirschner[1], E. Wang[1], F. Effenberg[3], D. Borodin[1], M.X. Navarro[4], H. Xie[5], M. Groth[6], H. Kumpulainen[6], K. Schmid[7], R.A. Pitts[8], A. Terra[1], A. Knieps[1], Y. Gao[9], M. Krychowiak[9], A. Pandey[9] and Ch. Linsmeier[1]

[1] Forschungszentrum Jülich GmbH, Institut für Energie- und Klimaforschung—Plasmaphysik, Partner of the Trilateral Euregio Cluster (TEC), 52425 Jülich, Germany
[2] Faculty of Mathematics and Natural Sciences, Heinrich Heine University Düsseldorf, 40225 Düsseldorf, Germany
[3] Princeton Plasma Physics Laboratory, Princeton, NJ, United States of America
[4] University of Wisconsin-Madison, Madison, WI, United States of America
[5] Institute of Plasma Physics Chinese Academy of Sciences, Hefei, China
[6] Aalto University, Espoo, Finland
[7] Max-Planck-Institut für Plasmaphysik, Garching b. München, Germany
[8] ITER Organization, Route de Vinon sur Verdon, Saint Paul Lez Durance, France
[9] Max-Planck-Institut für Plasmaphysik, 17491 Greifswald, Germany
[10] JARA-HPC, Jülich Supercomputing Centre, Forschungszentrum Jülich GmbH, Jülich 52425, Germany

E-mail: j.romazanov@fz-juelich.de

Received 15 January 2024, revised 17 May 2024
Accepted for publication 3 June 2024
Published 20 June 2024

Abstract

The paper provides an overview of recent modelling of global material erosion and deposition in the fusion devices Wendelstein 7-X (W7-X), JET and ITER using the Monte-Carlo code ERO2.0. For validating the modelling tool in a three-dimensional environment, W7-X simulations are performed to describe carbon erosion from the graphite test divertor units, which were equipped in operational phase OP 1.2 and analysed post-mortem. Synthetic spectroscopy of carbon line emission is compared with experimental results from the divertor spectrometer measurement system, showing a good agreement in the e-folding lengths in the radial intensity profiles of carbon. In the case of metallic wall materials, earlier modelling of the Be/W environment in JET and ITER is revisited and extended with an updated set of sputtering and reflection data, as well as including the mixing model for describing the Be/W dynamics in the divertor. Motivated by recent H/D/T isotope experiments in JET, limited and diverted configuration pulses are modelled, showing the expected trend of both Be and W erosion increasing with isotope mass. For the JET diverted configuration pulses, it is shown that Be

---

[*] Author to whom any correspondence should be addressed.

migrates predominantly to the upper part of the inner divertor where it initially leads to strong W erosion. With longer exposure time, the growth of a Be deposited layer leads to a reduction of W erosion in that region. A similar trend is observed in simulations of the ITER baseline $Q = 10$ scenario, however with a more symmetric Be migration pattern leading to deposition also on the outer divertor.

Keywords: ERO2.0, ITER, JET, W7-X, plasma impurity migration, erosion

(Some figures may appear in colour only in the online journal)

1. Introduction

Plasma-wall interaction (PWI) processes like erosion or fuel retention are a challenge for efficient and safe long-term operation of fusion devices like ITER. Computer code simulations of these processes are thus important for the design of future reactors, as well as for interpretation of experimental results. The three-dimensional (3D) Monte-Carlo code ERO2.0 [1] allows simulations of the material erosion under ion or charge-exchange (CX) neutral impact, as well as following the migration paths of eroded impurities through the plasma, including atomic and molecular processes like ionisation/recombination/dissociation, and secondary PWI processes like impurity re-deposition/re-erosion. The present contribution provides an overview of the recent validation of ERO2.0 using results from Wendelstein 7-X (W7-X) and JET experiments, and an update of predictions for ITER with respect to earlier ones published in [2].

2. W7-X modelling of C erosion and transport

Non-axisymmetric plasma shapes and geometries are important to take into account in PWI simulations, especially in view of the complex 3D magnetic topologies and plasma footprints induced by resonant magnetic perturbations planned to be used in ITER [3]. This necessitates experimental validation in fully 3D topologies, such as in the stellarator W7-X. The present modelling focuses on operational phase OP 1.2 of W7-X, which featured an island divertor consisting of passively cooled test divertor units (TDUs) with graphite as plasma-facing material [4]. For simulating global carbon (C) migration, we use a EMC3-EIRENE H plasma solution in standard magnetic configuration [5] as input to ERO2.0, which calculates C erosion and redeposition. The results are compared with spectroscopy profiles from [6] for attached conditions obtained from pulse #20181010.33 @1.0 s, a discharge in standard magnetic configuration with 4 MW input power, radiated fraction of 40% and an upstream density of 2×10^{-19} m^{-3}.

ERO2.0 is used to simulate the erosion and transport of carbon, using the EMC3-EIRENE plasma solution as a constant input. The erosion source takes into account physical sputtering by hydrogen (H) impact from the background plasma and carbon self-impact, as well as chemical sputtering by hydrogen impact. Physical sputtering yields are obtained from the binary collision approximation (BCA) code SDTrimSP [7] for a wide range of possible impact energies and angles, of which some are exemplarily shown in figures 1(*a*) and (*b*). The ion impact energies are set to $E = 2T_i + 3qT_e$ [8] and the impact angle with respect to the surface normal is set to 40°, the latter being an approximation of the typical mean impact angle of ions on a rough surface as discussed in [9]. Chemical erosion is calculated using the Roth formula [10] and assumed to preferentially release CH_4 molecules. Apart from the impact energy, the formula depends on the surface temperature T_{surf} and (less strongly) on the ion flux Γ. The former is obtained from experimental infra-red camera images [11] and is around $T_{\mathrm{surf}} \sim 500$ K in the plasma footprint region where most erosion occurs (with local hot spots of up to ~800 K and higher, see [4]). The ion flux is derived from EMC3-EIRENE and is around $\Gamma \sim 1 \times 10^{22}$ at m^{-2} s^{-1} in the plasma footprint region (see [4]). As discussed previously in [12], C erosion by H at low impact energies (<100 eV) is dominated by chemical erosion, which is illustrated in figure 2. Finally, it should be noted that the influence of impurities other than carbon on sputtering is neglected in the modelling, in particular oxygen is neglected corresponding to the conditions after a fresh boronization.

Hydrocarbon and carbon ions are followed through the plasma using the adaptive guiding center approximation (AGCA) method described in [13], which uses full orbit (FO) ion trajectory resolution only in specific regions e.g. close to PFCs, with a time constant of $dt = 100$ ns. It was verified for the W7-X setup that AGCA is faster while introducing no significant changes compared to using pure FO, the latter requiring significantly smaller time constants. The hydrocarbon molecular ionisation and dissociation chain is implemented as in ERO [14] using coefficients from [15]. Upon surface impact, the erosion induced by hydrocarbons is approximated by the sum of the erosion that would be induced by the molecule constituents carrying a fraction of the kinetic energy. Reflection probabilities of hydrocarbons are assumed to be 100% (zero sticking) for neutral hydrocarbons and 50% for hydrocarbon radicals according to the ‘standard assumptions’ mentioned in [16]. For atomic carbon, ionisation and recombination processes are modelled using ADAS coefficients [17], and reflection coefficients are calculated with SDTrimSP (figures 1(*c*) and (*d*)).

Before discussing the ERO2.0 simulation results, the applicability of the input EMC3-EIRENE solution to the plasma conditions present during spectroscopy measurements is verified by comparison with divertor Langmuir probe (LP)

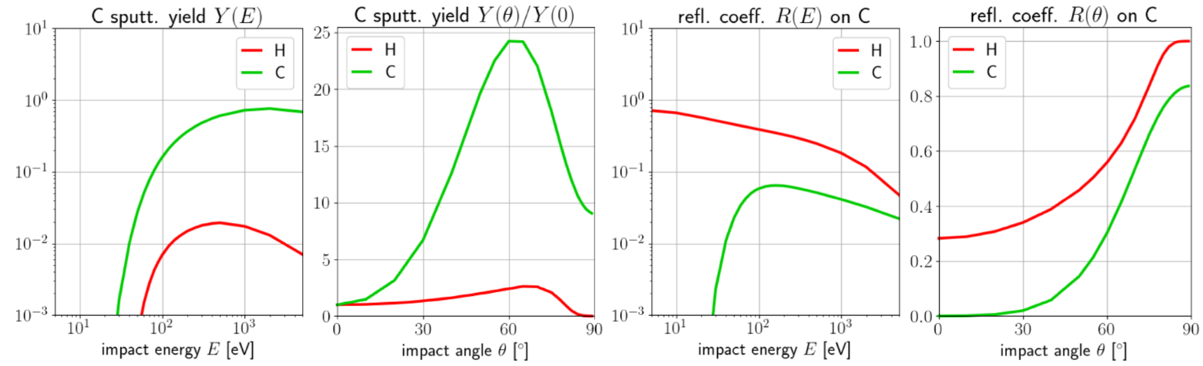

(a) **(b)** **(c)** **(d)**

Figure 1. Physical sputtering and reflection data for C targets calculated with SDTrimSP for different projectile species. Curves are shown for exemplary chosen impact energies and angles. (*a*) C sputtering yield, plotted over the impact energy at constant 40° impact angle. (*b*) C sputtering yield (normalized to the normal incidence yield), plotted over the impact angle at constant 100 eV impact energy. (*c*) Particle reflection coefficient on C targets, plotted over the impact energy at constant 40° impact angle. (*d*) Particle reflection coefficient on C targets, plotted over the impact angle at constant 100 eV impact energy.

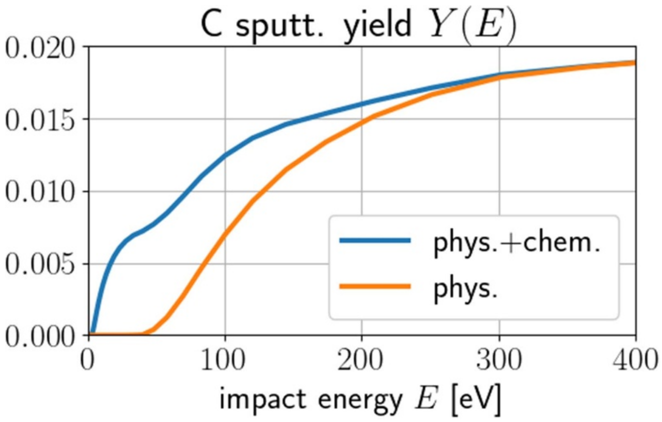

Figure 2. Carbon sputtering by hydrogen: influence of chemical erosion for typical divertor conditions considered in the simulations. The lower curve shows the physical sputtering yield by SDTrimSP at an impact angle of $\theta = 40°$, the upper curve adds the chemical according to the Roth formula [10] with surface temperature $T_{\text{surf}} = 500$ K and ion flux $\Gamma = 10^{22}$ at m^{-2} s^{-1}. See also [12].

measurements. The location of the LPs on the TDU is shown in figure 3(*a*) as cyan dots, together with green lines indicating the spectroscopy system sightlines, which observe radially outward and through the pumping gap between the horizontal and vertical targets. Figures 3(*b*) and (*c*) show the n_e and T_e values of the LPs with error bars. The average absolute deviation of simulated values from experimental ones is 28% for n_e and 19% for T_e. In the case of n_e, one can see the experimental values being consistently higher than the simulated ones. The simulated profile is also more smooth, while the experimental one shows a peak at LP channel 6 with a more than 2 times higher than the corresponding simulated value. As discussed in [18], error fields and drift effects are a main source of uncertainty in the EMC3-EIRENE simulations. A discussion of the influence of n_e, T_e profile uncertainties within a factor 2 is provided further below.

Carbon emission from both simulation and experiment shows a radial decay of the intensity with two distinct e-folding length regions. The simulated emission is obtained from 3D particle densities of CH, C^{+} and C^{2+} shown in figure 4, which are used to generate signals for the CH A-X Gerö band [19] at 431.0 nm and the emission lines C II at 426.7 nm and C III at 465.0 nm respectively. The density for CH is the lowest and the one for C^{2+} is the highest. Differences in density are partially due to different ionisation lengths for CH, C^{+} and C^{2+} (and the additional dissociation channel in the case of CH), and partially by the influence of reflection and re-erosion.

The 3D particle densities are converted to photon emissivities using coefficients from ADAS in the case of the C II and C III signals, and from IPProg [20, 21] in the case of the CH band signal. Note that the CH band is approximated by the main diagonal transition $v' = v'' = 0$, higher diagonal and off-diagonal transitions have lower contributions [20, 22] and are neglected here. The photon emissivities are subsequently integrated along the sightlines as described in [23]. The resulting emission profiles are shown in figure 5, where each measurement point corresponds to the emission integrated in one sightline, together with the corresponding experimental measurements from [6]. In general, both experiment and simulation qualitatively show a strong decay of the emission in the region near the target ($\lesssim$5 cm) followed by a constant signal far from the target ($\gtrsim$7 cm). A possible explanation for the kink is that sightlines which are located far from the horizontal target are passing through the vertical target (see figure 3(*a*)), with carbon from the vertical target producing the background signal.

In the region near the horizontal target (shaded area at 2–5cm), the simulated and experimental emission are in reasonable agreement (ratio within factor x3.2 for CH, x2.2 for C II and x1.7 for C III). Emission e-folding lengths obtained by exponential fitting in this area are comparable as well: $\lambda_{\text{exp}} = 0.97$ cm and $\lambda_{\text{sim}} = 0.92$ cm for CH, $\lambda_{\text{exp}} = 1.21$ cm and $\lambda_{\text{sim}} = 1.02$ cm for C II, $\lambda_{\text{exp}} = 1.55$ cm and $\lambda_{\text{sim}} = 1.39$ cm for C III. Note that the simulated C II and C III profiles show a distinct drop in the intensity very close to the target (<2 cm), which is

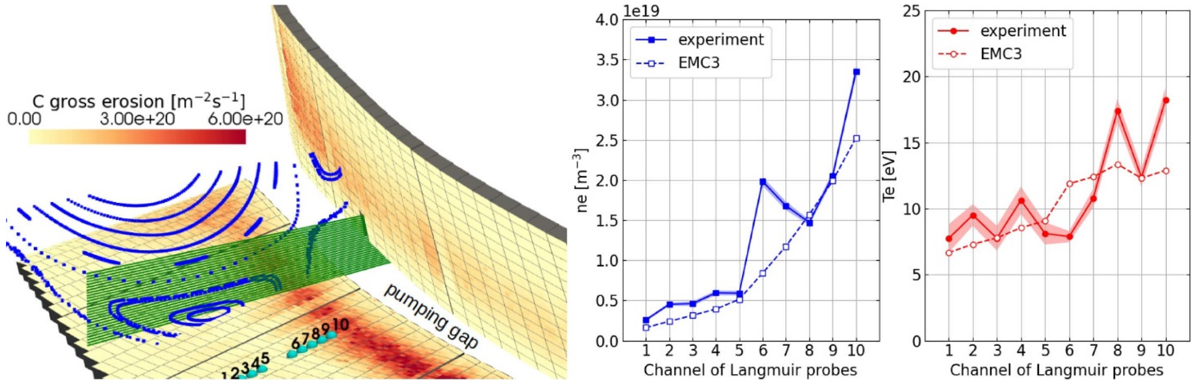

(a) (b) (c)

Figure 3. (*a*) W7-X simulation geometry of the TDU lower half-module, with C erosion patterns simulated by ERO2.0. Blue points (Poincaré plot) indicate the standard magnetic configuration topology. Green lines indicate the divertor spectrometer sightlines, observing from right to left through the pumping gap between horizontal and vertical divertor targets. Cyan dots indicate the Langmuir probe (LP) locations. (*b*) and (*c*) W7-X TDU LP measurements for discharge #20 181 010.33 @1.0 s [6], averaged in a ±5 ms window, compared with EMC3-EIRENE plasma parameters evaluated at the LP locations. The first channel is the furthest away from the pumping gap and vice versa.

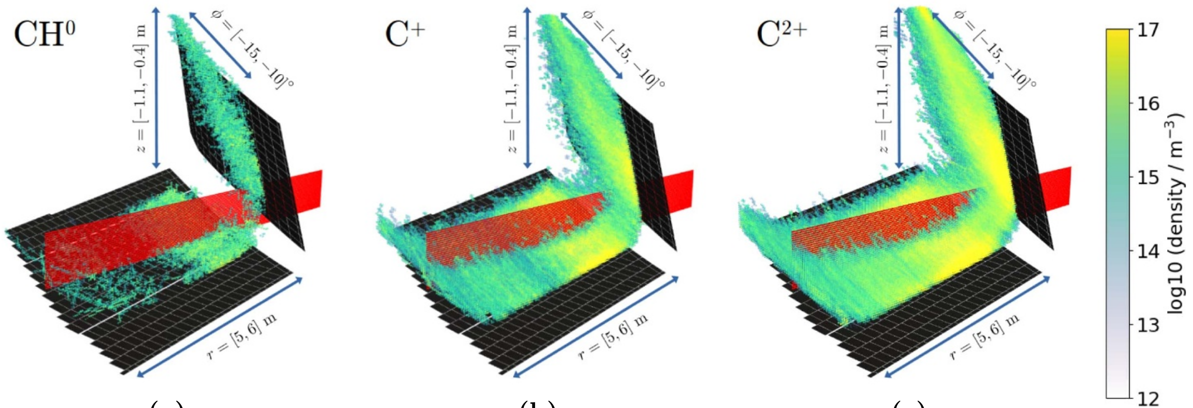

(a) (b) (c)

Figure 4. W7-X carbon particle densities in 3D, simulated with ERO2.0 and used for producing synthetic spectroscopy signals, shown together with the spectrometer sightlines (red). The plotted densities are clipped to the *r*, *phi* and *z* ranges indicated by the arrows for better visibility. (*a*) CH, (*b*) C^+, (*c*) C^{2+}. Additionally, transparency is added to low densities as indicated by the colorbar.

not observed in the experiment. On the simulation side, this region is very sensible both to small errors in the assumed coordinates of the spectroscopy sightlines and to the finite grid resolution (proximity of ‘empty’ grid cells just below or crossing the targets), which may explain the differences.

In the region far from the horizontal target, the experimental CH signal is too weak to be fitted since the molecules are already dissociated or ionised. Therefore, only C II and C III can be compared with simulations. In both cases the simulated emission is significantly lower than the experimental one, with factor x10.2 difference for C II and factor x3.4 difference for C III. This indicates an underestimation of erosion from the vertical target in the simulations. Another possible source of uncertainty are the plasma profiles, which affect the photon emissivity coefficients as well as the mean free paths for ionisation and dissociation. However, matching all emission simultaneously by adjusting the plasma parameters alone seems not possible. For example, reducing both n_e and T_e everywhere by factor 2 leads to a better agreement in the far region for C II but simultaneously to larger differences for C III. On the other hand, differences in the poloidal target profiles as observed in figures 3(*b*) and (*c*), such as the n_e peak in the experimental profile, can be to some extent smoothened out during the light integration in horizontal direction. Additional uncertainties can play a role in this region due to the low signals, for example background emission or light reflection from the baffle.

Another source of discrepancy are the absence of electric fields and temperature gradient forces in the current simulations. Due to numerical restrictions, EMC3-EIRENE does not provide the electric field. It was shown that drifts cause up-down asymmetries the particle fluxes on the TDUs [24], which in turn may cause the experimentally observed asymmetries in erosion/deposition patterns ([4] reports a difference in C net erosion of 40% between top and bottom TDUs in one half-module). The current simulations assume perfect up-down symmetry in the particle fluxes and plasma parameters. Furthermore, the ERO2.0 current simulations use a built-in

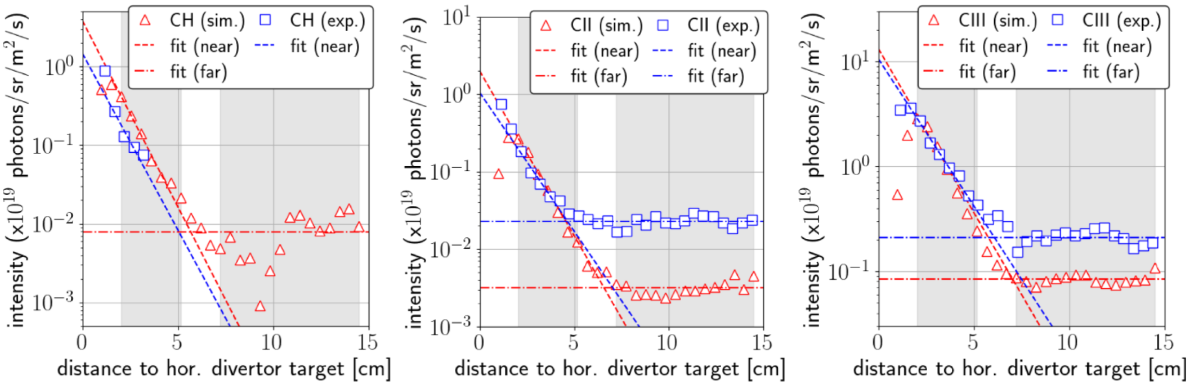

(a) **(b)** **(c)**

Figure 5. W7-X carbon emission: comparison between experimental signals for #20 181 010.33 @1.0 s [6] and simulated spectrometer signals. (*a*) Gerö molecular band at 431.0 nm, (*b*) C II line emission at 426.7 nm, (*c*) C III line emission at 465.0 nm. Both experimental and simulated values are fitted exponentially in two regions near (<5 cm) and far (>7 cm) from the divertor target, which are indicated by the two shaded areas in each plot.

model only for the sheath and pre-sheath electric field [25]. Compared to the experimental spectroscopy, the lack of $E \times B$ drifts outside the sheath affects the C transport and self-sputtering source, and in particular the C II and C III line emission. Temperature gradient forces (thermoforces) on the other hand are included in EMC3-EIRENE and generally have the effect of pushing particles away from divertor targets [26, 27]. In ERO2.0, thermoforces were implemented only recently [28] and were not available for the present study due to technical reasons.

Overall, the spectroscopy comparison is encouraging as a validation for the 3D modelling workflow, but also motivates further more detailed investigation on the influence of the photon emissivity coefficients, or more generally the rate coefficients for the hydrocarbon dissociation and ionisation chain, as well as $E \times B$ and thermoforce effects, which may be subject of future studies.

3. JET and ITER modelling of Be and W erosion and transport

The tokamak JET is equipped with an ITER-like wall, featuring beryllium (Be) in the first wall and tungsten (W) in the divertor, to enable PWI studies in preparation of ITER. Simulations of Be/W dynamics are therefore important for general validation of the code using JET results as well as predictions for ITER. Furthermore, understanding Be migration may be used as a proxy for predicting the behavior of low Z impurities in full-W devices, such as boron (B) from boronization which is used as alternative material for wall conditioning [29, 30]. Unless otherwise stated, the JET and ITER simulations described below are performed with similar assumptions as the ones above for W7-X.

3.1. Updated sputtering and reflection data

Previous ERO and ERO2.0 modelling studies for JET and ITER, such as [1, 2], used a set of Be sputtering data initially introduced in 2013 [31]. To account for the influence of fuel content in the surface (which is not directly tracked by the codes), those sputtering data are parametrized using the so-called 'ERO-max' and 'ERO-min' assumptions. The former are obtained with a pure Be surface, whereas the latter are obtained using 50% D fuel content in the surface, leading to generally lower sputtering yields.

New and more detailed ERO2.0 simulations of the recent JET experimental campaigns, considering different isotope plasmas (H/D/T) as well as Be/W mixed layer dynamics, were enabled by dedicated SDTrimSP calculations of sputtering and reflection data with a high resolution of impact energies and angles. Figure 6 shows the SDTrimSP sputtering and reflection coefficients for different projectiles on pure Be and W targets (He projectiles are included as additional information, but were not considered in the ERO2.0 simulations). For consistency with previous studies, an additional set of Be sputtering and reflection data was produced under the 'ERO-min' assumption with respective 50% H/D/T surface content. Figures 7(*a*) and (*b*) shows the Be 'ERO-min' and 'ERO-max' sputtering yields for H/D/T projectiles, including also the data from [31] (D only) for comparison. The new set of sputtering yields provides some improvements compared to the previous data. In particular, the 'ERO-min' curves in figure 7(*b*) show a strong reduction of yields for grazing incidence (impact angles $\theta \sim 90°$) compared to [31], which is considered more realistic and was achieved by improved assumptions for surface binding energy and atomic densities [32]. Note that the SDTrimSP data do not consider chemically assisted physical sputtering effects. This may be improved in the future by combining BCA data with molecular dynamics simulations for Be irradiation by H/D/T projectiles.

3.2. JET limited configuration pulses

JET limited configuration pulses have been used previously [33] to experimentally determine effective Be sputtering yields Y_{eff} in D plasma via spectroscopy, and were compared with Y_{eff} values from respective simulations (see e.g. [1]).

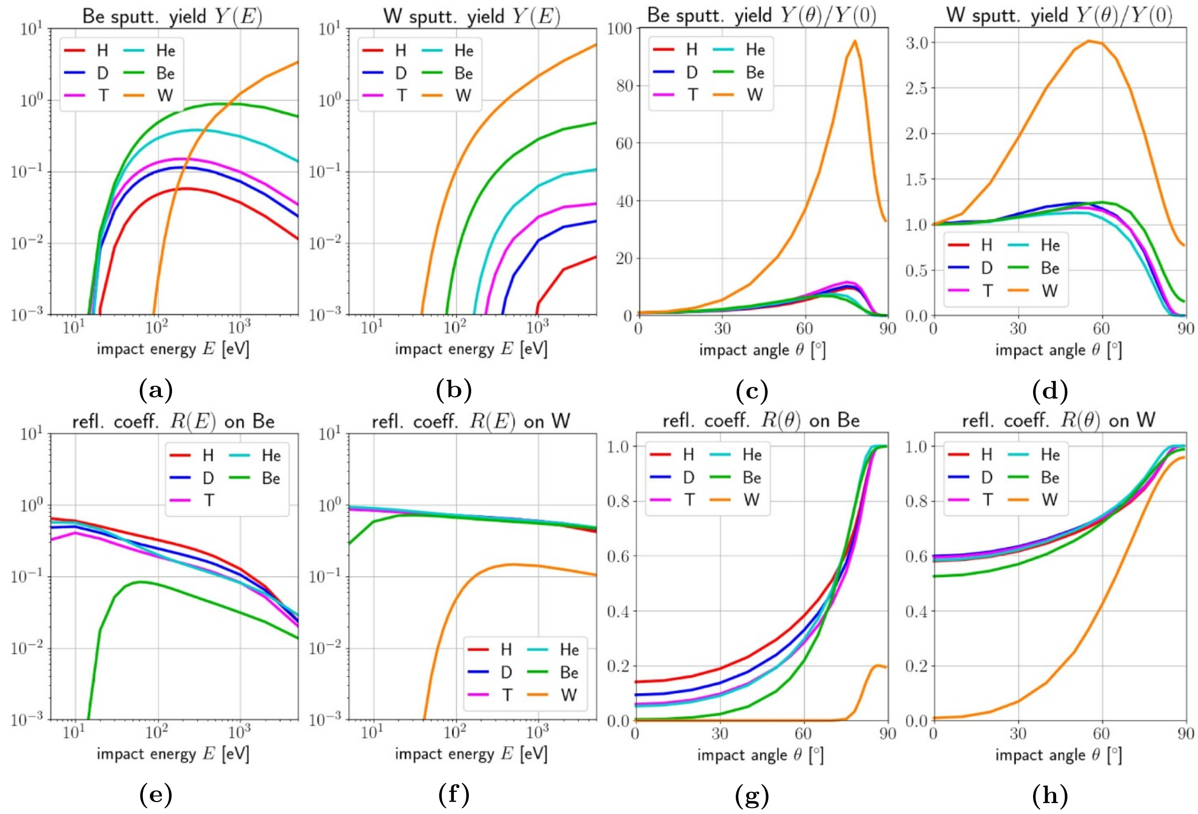

(a) (b) (c) (d)

(e) (f) (g) (h)

Figure 6. Physical sputtering and reflection data for Be and W targets calculated with SDTrimSP for different projectile species. Curves are shown for exemplary chosen impact energies and angles. (*a*) and (*b*) Be and W sputtering yield, plotted over the impact energy at constant 40° impact angle. (*c*) and (*d*) Be and W sputtering yield (normalized to the normal incidence yield), plotted over the impact angle at constant 300eV impact energy. (*e*) and (*f*) Particle reflection coefficient on Be and W targets, plotted over the impact energy at constant 40° impact angle. In (*e*), reflection is zero for W on Be in the entire plot range. (*g*) and (*h*) Particle reflection coefficient on Be and W targets, plotted over the impact angle at constant 300eV impact energy.

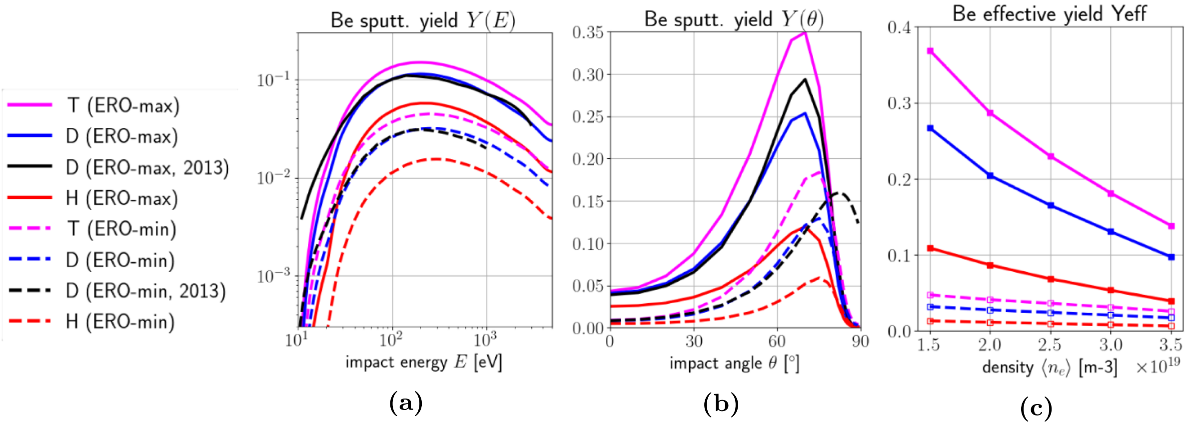

(a) (b) (c)

Figure 7. Sputtering yields for H/D/T projectiles on Be targets: influence of the hydrogen isotope surface content. Shown are the SDTrimSP yields obtained with a pure Be surface ('ERO-max', same as above in figure 6) and a hydrated surface with an assumed 50% content of H/D/T ('ERO-min'). The previously used '2013' set of data for D projectiles [31] is shown for comparison. (*a*) Energy dependence at constant 40° impact angle. (*b*) Angular dependence at constant 100 eV impact energy. (*c*) Effective sputtering yield obtained as the surface average in the spectroscopy observation spot on the JET inner wall guard limiter, for varying line-integrated density $\langle n_e \rangle$ (fuelling scan).

Recent JET experiments aimed at repeating these pulses with H and T plasma to study the isotope effect on erosion [34, 35]. The analysis of edge plasma parameter profiles for the respective pulses, needed as input for ERO2.0 modelling, is still ongoing so that a direct comparison between experiment and simulation was not possible for the present study. However, a simplified proof-of-concept modelling study was performed using the D plasma backgrounds from [1] and repeating for H and T by assuming the same plasma parameters and only changing the sputtering/reflection data to H and T respectively.

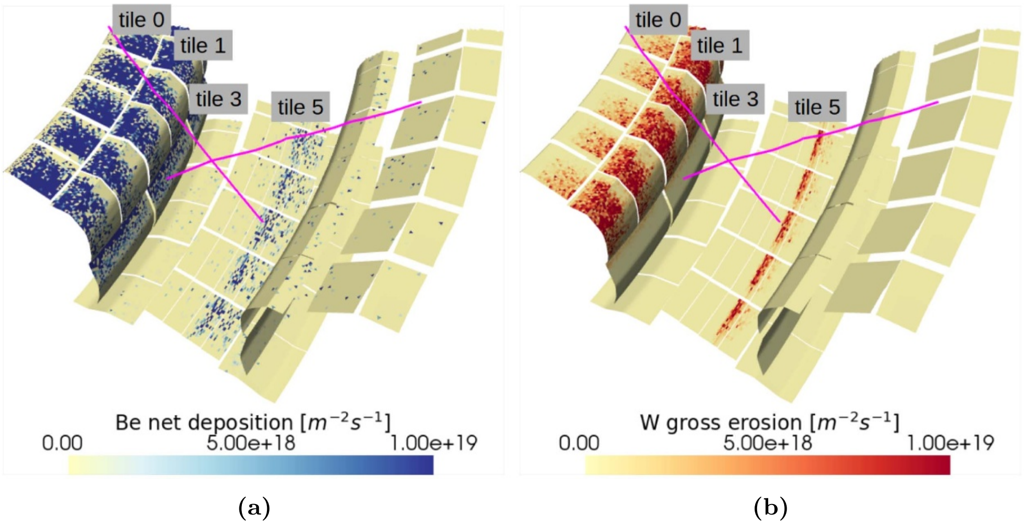

(a) **(b)**

Figure 8. JET divertor during H-mode configuration inter-ELM D plasma exposure with outer strikepoint on the bulk W target (tile 5). (*a*) Be net deposition flux. (*b*) W gross erosion flux.

The result is shown in figure 7(*c*), which shows the trend of Y_{eff} decreasing with increasing plasma line-averaged density $\langle n_e \rangle$ (corresponding to lower plasma temperatures thus impact energies), and increasing with the isotope mass as qualitatively confirmed by the recent experiments [34, 35]. At high densities (low impact energies), the ratio of sputtering for H:D:T is roughly proportional to the mass ratio 1:2:3. At low densities (high impact energies), the sputtering ratio is somewhat higher. This non-linearity is attributed to the influence of Be self-sputtering present in these plasma conditions, which is lowest for H ERO-min at high density (10% of total Be erosion) and highest for T ERO-max at low density (60% of total Be erosion).

3.3. JET diverted configuration pulses

The attached H-mode D plasma inter-ELM conditions from [1] ($B_t = 2.0\,\text{T}$, $I_p = 2.0\,\text{kA}$, $P_{\text{aux}} = 6.0\,\text{MW}$, $n_{e,\text{core}} = 6.5 \times 10^{19}\,\text{m}^{-3}$, $T_{e,\text{core}} = 1.8\,\text{keV}$, outer strikepoint on bulk W target), with the plasma background and CX neutral fluxes obtained from EDGE2D-EIRENE [36, 37], were revisited in this study and extended to H and T, again using the simplified assumption of having the same plasma conditions and only changing the sputtering/reflection data. Note that in contrast to earlier studies, the Be deposition and re-erosion in the divertor are now taken into account using the homogeneous mixing model (HMM) [38]. The time-dependent simulations start with a pure W divertor, and then evolve the surface material concentrations with a step length of 50–100 ms and a surface interaction layer of 5 nm thickness (based on SDTrimSP range calculations performed for Be and W targets and projectiles in the relevant impact energy range). It should be noted that other studies [39] use starting Be/W concentrations based on global modelling and post-mortem analysis instead of starting with a pure W divertor. The former is a more realistic approach for comparing with experiments, whereas the approach chosen here allows proof-of-concept studies on the initial dynamics of Be layers in the divertor. Note that the influence of intra-ELM conditions is neglected here. Taking those into account would change the erosion/deposition patterns. Importantly, sputtering by hydrogen isotopes is strongly increased during ELMs due to their energy increasing significantly beyond the W sputtering threshold [40]. A further important effect of ELMs is the influence of W transport into and from the main plasma, which was recently subject of dedicated global modelling studies [39]. Finally, as discussed above in section 2, thermoforces were not considered in the simulations. Taking these into account would reduce W redeposition as shown by local modelling [40], and can be expected to reduce the Be flux into the divertor.

The new simulations with H/D/T plasma show similar patterns of erosion and deposition in the divertor, with only the magnitude of both increasing with isotope mass [35], indicating that the main influence of the isotope is in the sputtering yields while transport patterns largely remain identical. Figure 8 exemplarly shows the 3D patterns of erosion and deposition in the divertor for a D plasma after $\Delta t = 1\,\text{s}$ exposure time and with the 'ERO-min' assumption. Figure 9 shows the corresponding 2D plots of Be and W impurities in the plasma. As seen in figure 8(*a*), Be eroded from the main chamber migrates predominantly into SOL and far-SOL regions of the inner divertor (tiles 0, 1, 3), leading to prominent Be net deposition zones. The deposition patterns are toroidally asymmetric due to shadowing effects of neighboring tilted divertor tiles. This is in line with post-mortem analysis which finds significant Be deposits of several μm thickness on tiles 0, 1, 3, thus posing the largest net deposition area in JET [41]. In the outer strikeline region (horizontal tile 5), a stripe of Be net deposition is observed in the PFR, which rapidly depletes in the SOL.

Since the divertor is assumed to start with pure W layers in the simulations, all regions of Be influx initially lead to W gross erosion in the inter-ELM conditions studied here, as seen in figure 8(*b*). After a certain exposure time (about 4 s in the

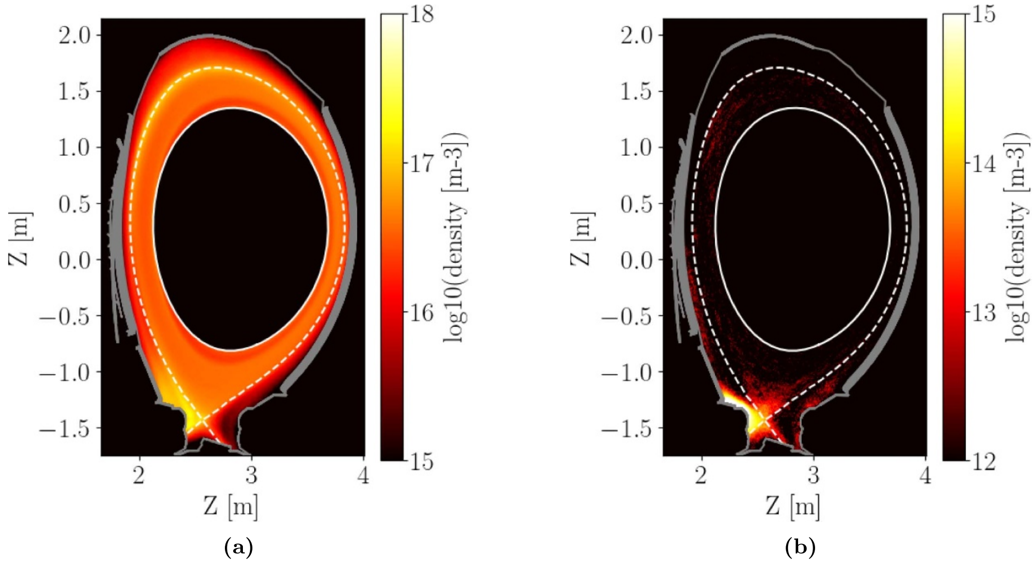

Figure 9. Toroidally averaged impurity density in JET (conditions as in figure 8): (*a*) Be, (*b*) W.

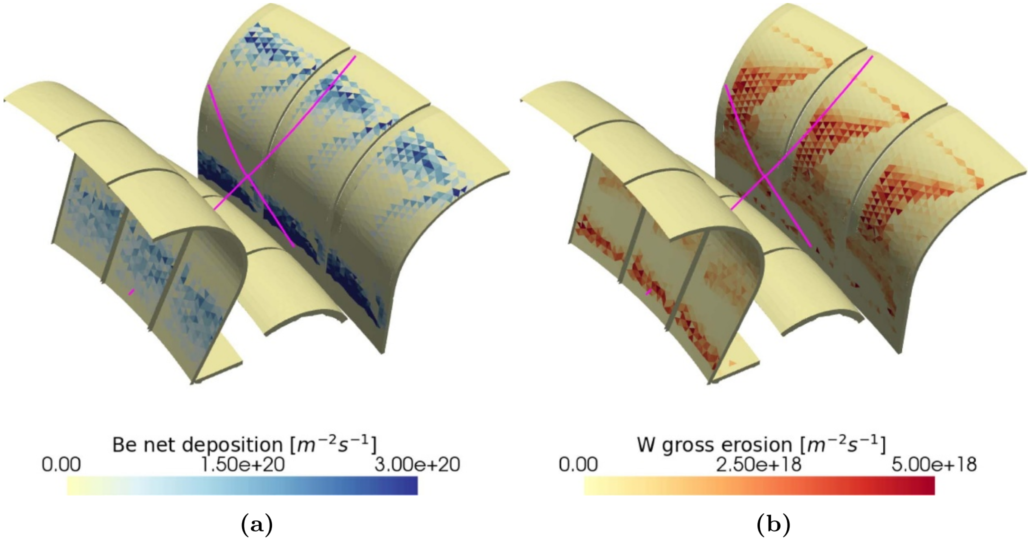

Figure 10. ITER divertor during $Q = 10$ H-mode baseline D-T inter-ELM plasma exposure. (*a*) Be net deposition flux. (*b*) W gross erosion flux.

ERO-min case shown in figure 8), a steady-state Be concentration is reached, reducing the W gross erosion in regions of net Be deposition compared to the initial clean W targets. Note that a high fraction of W is redeposited near the erosion location, as discussed e.g. in [42]. The W net erosion patterns (not shown here) are therefore close to zero on average, and subjected to strong Monte-Carlo noise, with no distinct net erosion or deposition zones. Finally, it should be noted that the influence of H/D/T CX neutrals on W erosion may be underestimated in the present study, since these are treated via their mean energies, which are provided by EDGE2D-EIRENE. These mean energies include also recycled neutrals. The mean energies in the divertor are too low to cause W erosion. A necessary improvement is to use information from energy spectra calculated with the EIRENE code. Taking these into account was shown to induce an additional, poorly screened erosion zone on the outer vertical target from which W can easily reach the core plasma [39]. Improved understanding of CX neutrals on PWI is topic of current research [43, 44].

3.4. *ITER baseline scenario*

Using the same updated code and sputtering/reflection data as for JET, we re-visit the ERO2.0 modelling of ITER $Q = 10$ semi-detached D-T discharges described in [2]. Here we use the OEDGE [45] set of plasma background and CX neutral fluxes labeled as ‘case #2’, which is defined by high far-SOL density and high SOL flow assumptions. In contrast to the earlier simulations, in which D plasma was assumed as a proxy for D-T, we now assume a 50%–50% D-T mix and use the new D and T sputtering/reflection data which leads to a more realistic description of the main erosion sources. Figure 10 shows

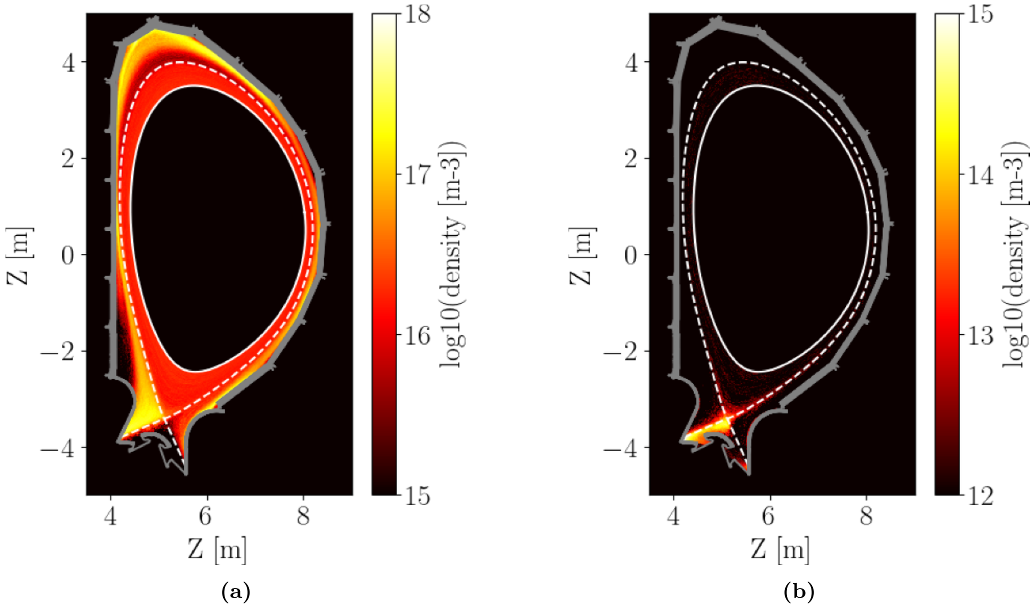

Figure 11. Toroidally averaged impurity density in ITER (conditions as in figure 10): (*a*) Be, (*b*) W.

3D patterns of erosion and deposition in the divertor, exemplarily for D plasma after $\Delta t = 12$ s exposure time and with the 'ERO-min' assumption. Figure 11 shows the corresponding 2D impurity densities of Be and W. Interestingly, the W SOL density is much lower compared to JET, which can be attributed to the higher density and consequently higher prompt redeposition. In contrast, the W density is high at the HFS PFR region due to the close vicinity of the W erosion region at the inner strikeline.

As for JET, one can see shadowing patterns in erosion and deposition due to the tilting between neighboring tiles [46]. In comparison to the JET case, the Be deposition in the inner divertor SOL is found closer to the strikeline. A prominent Be deposition zone is found on the top of the outer divertor, and an additional zone is formed with time just next to the outer strikeline. As for JET, the build-up of a steady-state Be concentration in certain divertor areas leads to a reduction of W erosion in these areas compared to the initial phase of the simulation with pure W targets. Compared to JET, the Be flux in ITER is higher in the outer divertor. One reason may be the relatively strong erosion on Be main chamber components in proximity to the outer divertor in ITER [2]. Additionally, differences in the background SOL flows can explain the differences in migration patterns. In ERO2.0 simulations, Be impurities in the SOL get entrained in the background flows (shown in figure 12 for the JET and ITER cases) after being eroded and ionised in the main chamber. The location of the stagnation region in the flow pattern (white-colored area on the low-field side in figure 12) determines whether they are ultimately deposited at the inner or outer divertor targets. The JET case features a stagnation region closer to the outer divertor, favouring counter-clockwise transport from the outer wall into the inner divertor. As explained in [2], the ITER OEDGE 'case #2' used here is already the one with the highest flows compared to other OEDGE cases. This means that in those other cases, the migration to the inner divertor in ITER is even weaker and potentially underestimated. This highlights the importance of correct understanding and modelling of SOL flows for predicting global migration.

4. Conclusions

Progress has been achieved in the validation of ERO2.0 in 3D environments (W7-X), with encouraging agreement between synthetic and experimental carbon emission. The comparison should be expanded using post-mortem analysis of the ^{13}C deposition from dedicated tracer experiment [4], which used similar plasma conditions as the ones considered here, and provides a means of validating local and global migration patterns. Corresponding ERO simulations are now in progress.

A large set of relevant SDTrimSP sputtering/reflection data needed for H/D/T isotope scans was produced and used for JET simulations. Effective yields were obtained for the limited plasma configuration, which are planned to be used for comparison with corresponding isotope experiments. Simulations of diverted configuration plasmas, with the HMM enabled to describe Be/W layer dynamics, qualitatively confirm the experimentally observed build-up of Be layers on top of the inner divertor, and demonstrate the important role of the main chamber Be source in the erosion of W targets. The experience from JET was extended to ITER predictions, which were updated using the mixing model and improved hydrogen isotope assumptions.

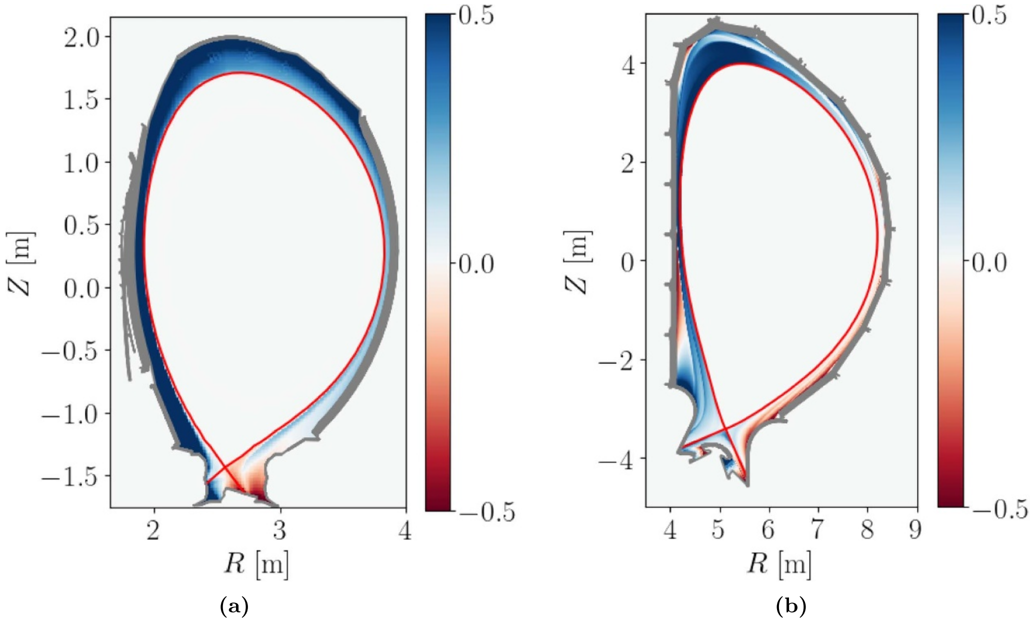

Figure 12. Background SOL flow velocity (Mach number) of D^+ ions in the (*a*) JET and (*b*) ITER cases. Data retrieved from EDGE2D-EIRENE and OEDGE respectively as input for ERO2.0. Positive (blue) = counter-clockwise, negative (red) = clockwise.

Acknowledgments

This work has been carried out within the framework of the EUROfusion Consortium, funded by the European Union via the Euratom Research and Training Programme (Grant Agreement No. 101052200—EUROfusion). Views and opinions expressed are those of the author(s) and do not necessarily reflect those of the European Union, the European Commission or the ITER Organization. Neither the European Union nor the European Commission can be held responsible for them. The authors gratefully acknowledge computing time on the supercomputer JURECA [47] at Forschungszentrum Jülich under Grant No. CJIEK43. This work was supported by the US DoE under Contract DE-AC02-09CH11466.

ORCID iDs

J. Romazanov https://orcid.org/0000-0001-9439-786X
S. Brezinsek https://orcid.org/0000-0002-7213-3326
C. Baumann https://orcid.org/0000-0001-7712-5379
S. Rode https://orcid.org/0009-0009-7614-5218
A. Kirschner https://orcid.org/0000-0002-3213-3225
F. Effenberg https://orcid.org/0000-0002-4846-4598
D. Borodin https://orcid.org/0000-0001-8354-1387
M.X. Navarro https://orcid.org/0000-0002-0267-7774
H. Xie https://orcid.org/0009-0000-0605-6089
M. Groth https://orcid.org/0000-0001-7397-1586
H. Kumpulainen https://orcid.org/0000-0003-1301-0497
R.A. Pitts https://orcid.org/0000-0001-9455-2698
A. Terra https://orcid.org/0000-0003-0638-6103
A. Knieps https://orcid.org/0000-0003-0083-7188
Y. Gao https://orcid.org/0000-0001-8576-0970
M. Krychowiak https://orcid.org/0009-0001-4141-5558
Ch. Linsmeier https://orcid.org/0000-0003-0404-7191

References

[1] Romazanov J. *et al* 2019 *Nucl. Mater. Energy* **18** 331–8
[2] Romazanov J. *et al* 2022 *Nucl. Fusion* **62** 036011
[3] Frerichs H., Bonnin X., Feng Y., Li L., Liu Y., Loarte A., Pitts R., Reiter D. and Schmitz O. 2021 *Nucl. Fusion* **61** 126027
[4] Brezinsek S. *et al* 2022 *Nucl. Fusion* **62** 082506
[5] Effenberg F. *et al* 2019 *Nucl. Fusion* **59** 106020
[6] Wang E. *et al* 2022 *Nucl. Mater. Energy* **33** 101283
[7] Mutzke A., Schneider R., Eckstein W., Dohmen R., Schmid K., von Toussaint U. and Badelow G. 2019 *Technical Report* IPP 2019-02 Max-Planck-Institut für Plasmaphysik, Garching, Germany
[8] Stangeby P.C. 2000 *The Plasma Boundary of Magnetic Fusion Devices* (IOP Publishing)
[9] Schmid K. 2022 *Nucl. Mater. Energy* **33** 101230
[10] Roth J. and Garcia-Rosales C. 1996 *Nucl. Fusion* **36** 1647–59
[11] Gao Y., Jakubowski M.W., Drewelow P., Pisano F., Sitjes A.P., Niemann H., Ali A. and Cannas B. (W7-X Team) 2019 *Nucl. Fusion* **59** 066007
[12] Schmid K. *et al* 2020 *Nucl. Mater. Energy* **25** 100821
[13] Rode S., Romazanov J., Reiser D., Brezinsek S., Linsmeier C. and Pukhov A. 2022 *Contrib. Plasma Phys.* **62** e202100172
[14] Kögler U. and Winter J. 1996 ERO-TEXTOR: 3D-montecarlo code for local impurity-modeling in the scrape-off-layer of TEXTOR *PhD Thesis* Universität Düsseldorf
[15] Janev R.K. and Reiter D. 2002 *Phys. Plasmas* **9** 4071
[16] Kirschner A. *et al* 2011 *J. Nucl. Mater.* **415** S239–45
[17] Summers H.P. and O'Mullane M.G. 2005 The atomic data and analysis structure *Nuclear Fusion Research: Understanding Plasma-Surface Interactions* vol 78 (Springer) pp 399–413
[18] Effenberg F. *et al* 2019 *Nucl. Mater. Energy* **18** 262–7
[19] Brezinsek S. *et al* 2007 *J. Nucl. Mater.* **363–365** 1119–28
[20] Celiberto R., Janev R.K. and Reiter D. 2009 *Plasma Phys. Control. Fusion* **51** 085012

[21] Fantz U. and Meir S. 2005 *J. Nucl. Mater.* **337–339** 1087–91
[22] Greenland P.T. and Brezinsek S. 2004 *Technical Report* JUEL-4156 (Forschungszentrum Jülich GmbH, Institut für Energie- und Klimaforschung—Plasmaphysik, Partner of the Trilateral Euregio Cluster (TEC))
[23] Romazanov J. *et al* (JET Contributors) 2017 *Phys. Scr.* **T170** 014018
[24] Hammond K.C. *et al* 2019 *Plasma Phys. Control. Fusion* **61** 125001
[25] Borodkina I., Borodin D., Kirschner A., Tsvetkov I.V., Kurnaev V.A., Komm M. and Dejarnac R. (JET Contributors) 2016 *Contrib. Plasma Phys.* **56** 640–5
[26] Feng Y., Sardei F., Grigull P., McCormick K., Kisslinger J. and Reiter D. 2006 *Nucl. Fusion* **46** 807
[27] Gradic D., Ford O.P., Burckhart A., Effenberg F., Frerichs H., König R., Lunt T., Perseo V. and Wolf R.C. 2018 *Plasma Phys. Control. Fusion* **60** 084007
[28] Mäenpää R. *et al* 2022 *Nucl. Mater. Energy* **33** 101273
[29] Krieger K., Balden M., Bortolon A., Dux R., Griener M., Hegele K., Laggner F., Rohde V. and Wampler W.R. 2023 *Nucl. Mater. Energy* **34** 101374
[30] Bodner G. *et al* 2022 *Nucl. Fusion* **62** 086020
[31] Borodin D. *et al* 2013 *J. Nucl. Mater.* **438** S267–71
[32] Schmid K. 2023 private communication
[33] Brezinsek S. *et al* 2015 *Nucl. Fusion* **55** 063021
[34] Borodkina I. *et al* 2023 *29th IAEA Fusion Energy Conf. (FEC 2023) (London, United Kingdom, 16–21 October 2023)* (available at: www.iaea.org/events/fec2023)
[35] Douai D. *et al* 2023 *29th IAEA Fusion Energy Conf. (FEC 2023) (London, United Kingdom, 16–21 October 2023)* (available at: www.iaea.org/events/fec2023)
[36] Simonini R., Corrigan G., Radford G., Spence J. and Taroni A. 1994 *Contrib. Plasma Phys.* **34** 368–73
[37] Reiter D., Baelmans M. and Börner P. 2005 *Fusion Sci. Technol.* **47** 172–86
[38] Navarro M. *et al* 2021 *63rd APS DPP Meeting* (*Pittsburgh, PA, 8–12 November 2021*) p O08.00007 (available at: https://meetings.aps.org/Meeting/DPP21/Content/4081)
[39] Kumpulainen H.A., Groth M., Brezinsek S., Casson F., Corrigan G., Frassinetti L., Harting D. and Romazanov J. (JET contributors) 2024 *Plasma Phys. Control. Fusion* **66** 055007
[40] Kirschner A. *et al* 2019 *Nucl. Mater. Energy* **18** 239–44
[41] Widdowson A. *et al* 2017 *Nucl. Mater. Energy* **12** 499–505
[42] Kirschner A., Tskhakaya D., Kawamura G., Borodin D., Brezinsek S., Ding R., Linsmeier C.C. and Romazanov J. 2016 *Contrib. Plasma Phys.* **56** 622–7
[43] Shi X.Z., Ding R., Matveev D., Mu L., Liu N.X., Xie H., Xu G.L. and Chen J.L. 2023 *Nucl. Fusion* **63** 066015
[44] Ren J. *et al* 2023 *Nucl. Mater. Energy* **37** 101523
[45] Lisgo S., Kukushkin A., Pitts R. and Reiter D. 2013 *J. Nucl. Mater.* **438** S580–4
[46] Pitts R.A. *et al* 2017 *Nucl. Mater. Energy* **12** 60–74
[47] Jülich Supercomputing Centre 2021 *J. Large-Scale Res. Facil.* **7** A182